ATLAS NOTE

ATLAS-CONF-2016-039

30th July 2016

Boosted Higgs ($\rightarrow b\bar{b}$) Boson Identification with the ATLAS Detector at $\sqrt{s} = 13$ TeV

The ATLAS Collaboration

Abstract

This document summarises the baseline boosted Higgs boson identification strategy for Run 2 data collected by the ATLAS detector at a centre-of-mass energy of $\sqrt{s} = 13$ TeV, as updated for the analysis of the 2015 and 2016 data. Boosted $H \rightarrow b\bar{b}$ decays are reconstructed from jets found with the anti-k_t $R = 1.0$ jet algorithm, that are trimmed using a subjet radius of $R_{\text{subjet}} = 0.2$ and a minimum transverse momentum fraction of $f_{\text{cut}} = 5\%$. To tag Higgs bosons, requirements are applied on the following quantities: b-jets identified using $R = 0.2$ track jets matched to the large-R calorimeter jet, the trimmed jet mass and the trimmed jet energy correlation ratio $D_2^{(\beta=1)}$. The Higgs boson tagging efficiency and corresponding multi-jet and hadronic top background rejections in simulated events are presented. Several benchmark tagging selections are defined based on specific signal efficiency targets. Systematic uncertainties on the Higgs tagging efficiency and background rejection resulting from uncertainties on the b-tagging efficiency, mass and $D_2^{(\beta=1)}$ variables are provided. In addition, the b-tagging performance at small b-quark angular separations and the modelling of the jet properties, including jet substructure variables, are tested in a high p_{T} $g \rightarrow b\bar{b}$ rich sample of large-R jets from pp collisions at $\sqrt{s} = 13$ TeV recorded in 2015.

ATLAS-CONF-2016-039
08 August 2016

1 Introduction

The increase of the LHC centre-of-mass energy to 13 TeV, and the increase in luminosity, greatly extends the sensitivity of the ATLAS experiment [1] to heavy new particles. In a significant number of new physics scenarios [2–4], these heavy new particles may have decay chains including the recently discovered Higgs boson [5, 6]. The large mass of these resonances implies that a large momentum will be imparted to the Higgs boson, causing the decay products of the Higgs boson to be collimated. The decay of the Higgs boson to $b\bar{b}$ pairs has the largest branching fraction within the Standard Model, and thus is a vital decay mode to use when searching for these resonances (see e.g. Ref. [7]), as well as for Standard Model Higgs boson precision measurements [8]. For high momentum, or boosted, Higgs bosons decaying to $b\bar{b}$ pairs, the signature will be a high momentum "Higgs-jet" containing two b-hadrons.

In order to identify, or tag, boosted Higgs-jets it is paramount to understand the details of b-hadron identification and the internal structure of jets, or jet substructure, in such an environment. The approach to Higgs-jet tagging presented in this note is built upon a strong foundation of studies from LHC Run 1, including extensive studies of jet reconstruction and grooming algorithms [9] and detailed investigations of track-jet-based b-jet identification in boosted topologies [10].

This note follows up on a previous study [11], by improving the expected mass resolution for Higgs boson decays selected in large-R jets, by refining the Higgs boson selection criteria, and by carrying out a data-to-simulation comparison of large-R jet properties. After a brief description of the ATLAS detector in Section 2 and of the data and simulated samples in Section 3, the selection as well as association of objects is discussed in Section 4, as is the scheme used to label the jets' truth flavour. The Higgs-jet tagging algorithm and its performance are presented in Section 5. Finally, Section 6 discusses a comparison between representative distributions in a control sample in data dominated by $g \to b\bar{b}$ and corresponding simulated events.

2 ATLAS detector

The ATLAS detector [1] at the LHC covers nearly the entire solid angle around the collision point.[1] It consists of an inner tracking detector surrounded by a thin superconducting solenoid, electromagnetic and hadronic calorimeters, and a muon spectrometer incorporating three large superconducting toroid magnets. The inner-detector system (ID) is immersed in a 2 T axial magnetic field and provides charged particle tracking in the range $|\eta| < 2.5$.

Preceding data taking at the increased centre-of-mass energy of 13 TeV, the high-granularity silicon pixel detector was equipped with a new barrel layer, located at a smaller radius than the existing layers (at about 34 mm). The upgraded detector covers the vertex region and typically provides four measurements per track, the first hit being normally in the innermost layer. It is followed by the silicon microstrip tracker which usually provides four two-dimensional measurement points per track. These silicon detectors are complemented by the transition radiation tracker, which enables radially extended track reconstruction up to $|\eta| = 2.0$. The transition radiation tracker also provides electron identification information based on the

[1] ATLAS uses a right-handed coordinate system with its origin at the nominal interaction point (IP) in the centre of the detector and the z-axis along the beam pipe. The x-axis points from the IP to the centre of the LHC ring, and the y-axis points upwards. Cylindrical coordinates (r, ϕ) are used in the transverse plane, ϕ being the azimuthal angle around the z-axis. The pseudorapidity is defined in terms of the polar angle θ as $\eta = -\ln\tan(\theta/2)$. Angular distance is measured in units of $\Delta R \equiv \sqrt{(\Delta\eta)^2 + (\Delta\phi)^2}$.

fraction of hits (typically 30 in total) above a higher energy deposit threshold corresponding to transition radiation.

The calorimeter system covers the pseudorapidity range $|\eta| < 4.9$. Within the region $|\eta| < 3.2$, electromagnetic calorimetry is provided by barrel and endcap high-granularity lead/liquid-argon (LAr) electromagnetic calorimeters, with an additional thin LAr presampler covering $|\eta| < 1.8$, to correct for energy loss in material upstream of the calorimeters. Hadronic calorimetry is provided by the steel/scintillating-tile calorimeter, segmented into three barrel structures within $|\eta| < 1.7$, and two copper/LAr hadronic endcap calorimeters. The solid angle coverage is completed with forward copper/LAr and tungsten/LAr calorimeter modules optimised for electromagnetic and hadronic measurements respectively.

The muon spectrometer (MS) comprises separate trigger and high-precision tracking chambers measuring the deflection of muons in a magnetic field generated by superconducting air-core toroids. The precision chamber system covers the region $|\eta| < 2.7$ with three layers of monitored drift tubes, complemented by cathode strip chambers in the forward region, where the background is highest. The muon trigger system covers the range $|\eta| < 2.4$ with resistive plate chambers in the barrel, and thin gap chambers in the endcap regions.

A two-level trigger system is used to select interesting events [12, 13]. The Level-1 trigger is implemented in hardware and uses a subset of detector information to reduce the event rate to a design value of at most 100 kHz. This is followed by the software-based trigger level, the High-Level Trigger (HLT), which reduces the event rate further to about 1 kHz.

3 Data and MC samples

The data used in this note were recorded with the ATLAS detector during the 2015 pp collision run, and correspond to a total integrated luminosity of 3.2 fb^{-1} at $\sqrt{s} = 13$ TeV. The uncertainty in the integrated luminosity is ±2.1%. It is derived, following a methodology similar to that detailed in Refs. [14] and [15], from a calibration of the luminosity scale using x-y beam-separation scans performed in August 2015. This integrated luminosity accounts for data quality requirements, which ensure that the ATLAS detector was operating well while the data were recorded. Events are required to have a primary vertex with at least 3 tracks associated, and the highest $\sum p_{\mathrm{T}}^2$ vertex is considered as the primary vertex. At HLT level, calorimeter jets are reconstructed using the same anti-k_t algorithm [16] (using $R = 0.4$) used offline (see Section 4); events are selected using single jet triggers with thresholds of 100, 150, 175, 200, 260, 300, 320 and 360 GeV. Events must have been recorded by the highest p_{T} trigger that is fully efficient for the leading p_{T} $R = 0.4$ offline jet in the event.

Several Monte Carlo (MC) simulated samples are used for the optimisation of the Higgs tagger, the estimation of its performance, and the comparison between data and simulation of its features.

A broad Higgs boson p_{T} spectrum, with $H \to b\bar{b}$, is generated as decay products of Randall-Sundrum gravitons of different masses in a benchmark model with a warped extra dimension [2]. The events are generated at leading order using the MadGraph5_aMC@NLO generator [17] interfaced with PYTHIA8 [18] for showering and hadronisation. The leading-order NNPDF2.3 parton distribution (PDF) set [19] is used, with the ATLAS A14 [20] tuned modelling of showering and underlying event parametrisations.

Samples of top quark pair events, with hadronically decaying top quarks, are generated using POWHEG [21, 22] interfaced to PYTHIA [23], and with the PERUGIA 2012 [24] underlying event tune parameter sets. Finally, an inclusive multijet sample is generated using PYTHIA8, with the leading-order NNPDF2.3 PDF set and the A14 underlying event tune parameter sets. EVTGEN [25] is used in all cases to model the decays of b- and c-flavoured hadrons.

4 Object selection, association and flavour labelling

The selection, the matching criteria or association, and the determination of the heavy flavour content of physics objects for this analysis are described below.

Calorimeter jets: The standard inputs to calorimeter jet reconstruction in ATLAS are topological clusters of calorimeter cell energy deposits [26]. The clusters are considered massless, and are calibrated using the local hadronic cell weighting method. Calorimeter jets reconstructed using FASTJET [27, 28] with the anti-k_t algorithm [16] with distance parameter $R = 1.0$ ("large-R" jets) and $R = 0.4$ ("small-R" jets) are used. The trimming algorithm [29], adopted by ATLAS as the standard grooming procedure for anti-k_t jets with $R = 1.0$, discards the softer components of the jet, including contributions from pile-up and underlying event. For trimming, k_t [30] subjets with $R_{\text{sub}} = 0.2$ are used with a minimum transverse momentum fraction $f_{\text{cut}} = 0.05$. After this grooming procedure, the jet energy and mass are calibrated using particle-level correction factors derived from simulation [31, 38]. Only jets with $p_{\text{T}} > 250$ GeV and pseudorapidity $|\eta| < 2.0$ are considered in this analysis.

Truth jets: Truth jets are built in simulated events from truth particles with lifetimes greater than 10 picoseconds, except for muons and neutrinos, which are not included. The same jet clustering algorithm used for the calorimeter jets is also used to reconstruct truth jets.

Track jets: Track jets are reconstructed from inner detector tracks using the anti-k_t algorithm with a distance parameter of $R = 0.2$ [10]. The tracks are required to have:

- $p_{\text{T}} > 0.4$ GeV and $|\eta| < 2.5$;
- at least 7 hits in the silicon detectors (pixel detector + silicon strip detector);
- no more than one hit in the pixel detector that is shared by multiple tracks;
- no more than one missing hit in the pixel detector, where a hit is expected, and no more than two missing hits in the silicon detectors, where a hit is expected;
- a tight match to the hard scatter vertex by requiring that the track is a constituent of the reconstructed hard scatter vertex, or the track longitudinal impact parameter with respect to the hard scatter vertex, z_0, satisfies $|z_0 \sin(\theta)| < 3$ mm, where θ is the the polar angle of the track momentum at the perigee.

Such requirements greatly reduce the number of tracks from pileup vertices whilst being highly efficient for tracks from the hard scatter vertex. Once the track jet axis is determined, a second step of track association is performed in order to collect tracks needed for effectively running the b-hadron identification algorithms described later in this section. Tracks are selected without impact parameter requirements but within a cone whose size depends on jet p_{T} [33]. Only track jets with $p_{\text{T}} > 10$ GeV, $|\eta| < 2.5$, and with at least two tracks are used for the analysis. The b-hadron identification efficiency of track jets is calibrated using Run 2 $t\bar{t}$ candidate data events.

Muons: Muons are reconstructed from a combination of measurements from the inner detector and the muon spectrometer. They are required to have ≥ 3 hits on at least two layers of monitored drift tubes (MDT), except for the $|\eta| < 0.1$ region where tracks with at least three hits in one single MDT layer are allowed. The difference between the inner detector and muon spectrometer $1/p$ measurements is required to be below 7 standard deviations. Muons selected for this analysis are required to have $p_{\mathrm{T}} > 10$ GeV and $|\eta| < 2.4$.

Ghost association: In events with a dense hadronic environment, there can often be an ambiguity when matching track jets to calorimeter jets. The track jet association to large-R jets is performed using ghost-association [34–36], which provides a robust matching procedure that makes use of the catchment area of the jet [36]. As a result, matching to jets with irregular boundaries can be achieved in a less ambiguous way than a simple geometric (i.e. ΔR between objects) matching. In this procedure, the "ghosts" are the track jet 4-vectors in the event, with the track jet p_{T} set to an infinitesimal amount, essentially only retaining the direction of the track jets. This ensures that jet reconstruction is not altered by the ghosts when the calorimeter clusters plus ghosts are reclustered. The reclustering is then performed using the anti-k_t algorithm with $R = 1.0$. The calorimeter jets after reclustering are identical to the ungroomed parents of the trimmed jets used in this analysis, with the addition of the associated track jets retained as constituents. In this analysis, track jets ghost-associated to the large-R jet refer to track jets found this way within the catchment area of the ungroomed parent jet, but the kinematics of the large-R jet are still measured using the trimmed jet.

Jet flavour labelling: The labelling of the flavour of the track jets in simulation is done by geometrically matching the jet with generator-level hadrons: if a weakly decaying b-hadron with $p_{\mathrm{T}} > 5$ GeV is found within $\Delta R < 0.2$ of the jet direction, where R is the jet distance parameter, the jet is labelled as a b-jet. In the case that the b-hadron could match more than one jet, only the closest jet is labelled as a b-jet. If no b-hadron is found, the procedure is repeated for weakly decaying c-hadrons to label c-jets. If no c-hadron is found, the procedure is repeated for τ leptons to label τ-jets. A jet for which no such association can be made is labelled as a light-flavour jet.

The flavour labelling for large-R jets is also important for this analysis to define the Higgs-jet signal and background efficiencies. Higgs-jets are defined as large-R jets with a truth Higgs boson and the corresponding two decay b-hadrons found within $\Delta R < 1$. Top jets are defined as large-R jets in which a truth top quark is found within $\Delta R < 1$ of the large-R jet axis.

b-jet identification: Several algorithms to identify b-jets have been developed based on the lifetime and decay properties of b-hadrons [33]. Tracks that are associated to the jets and that pass basic quality requirements are used as inputs to the algorithms. The algorithms use relatively simple impact parameter (IP3D) and secondary vertex (SV1) information, or, in the case of the more refined JetFitter algorithm, exploit the topology of weak b- and c-hadron decays using a Kalman filter to search for a common line connecting the primary vertex to beauty and charm decay vertices.

The MV2c10 algorithm [33, 37] employs a boosted decision tree based on jet properties and properties computed from IP3D, SV1 and JetFitter. It is trained with b-jets as signal, and a mix of approximately 93% light-flavour jets and 7% c-jets as background. The multivariate b-tagging algorithms have been trained using $R = 0.4$ calorimeter jets, but they are used for both calorimeter and track jets.

For a jet to be considered b-tagged, the output of the multivariate b-tagging algorithm is required to be above a fixed threshold value. Several such thresholds, or "working points" (WP), are defined, in such a way as to correspond to a well-defined average efficiency when applied to b-jets from a sample of

inclusive $t\bar{t}$ events. In this note, emphasis will be placed on WP that are tuned to an average 70% and 77% b-tagging efficiency.

Large-R jet mass: An independent estimate of the invariant mass of large-R jets, intended to overcome the limited angular resolution provided by the calorimeter, is obtained as the so-called "track-assisted jet mass" m^{TA} [38] which is computed as $m^{\mathrm{TA}} = m^{\mathrm{track}} \times p_{\mathrm{T}}^{\mathrm{calo}}/p_{\mathrm{T}}^{\mathrm{trk}}$, where m^{track} is the invariant mass of the tracks associated with the trimmed large-R jet reconstructed using the calorimeter, $p_{\mathrm{T}}^{\mathrm{calo}}$ is the transverse momentum of the trimmed large-R jet reconstructed using the calorimeter, and $p_{\mathrm{T}}^{\mathrm{track}}$ is the transverse momentum of the sum over the four-momenta of associated tracks. The correction factor $p_{\mathrm{T}}^{\mathrm{calo}}/p_{\mathrm{T}}^{\mathrm{track}}$ corrects for the neutral jet component, to which m^{track} is not sensitive. The track-assisted jet mass is calibrated using particle-level correction factors derived from simulation [38] as for calorimeter jets.

As shown in Figure 1(a), the resolution in the response to jet mass $R_m = m_{\mathrm{reco}}/m_{\mathrm{truth}}$ provided by m^{TA} is compared to the jet mass reconstructed using the calorimeter m^{calo} as a function of truth Higgs-jet p_{T}. The truth jet mass m_{truth} is the invariant mass of particles clustered into truth trimmed large-R jets. The relative jet mass resolution is defined as half the central 68% probability interval divided by the median of the jet mass response distribution. The m^{calo} observable provides better resolution than m^{TA} over the entire p_{T} range considered. Both the calorimeter-based and track-assisted jet mass resolution degrade for $p_{\mathrm{T}} > 800$ GeV. For m^{calo} this is due to the finite granularity of the calorimeter; for m^{TA} it is due to a degrading track momentum resolution and to a loss of tracks in the high density jet core caused by overlapping hits [38]. The tracks from the b-hadron decays are expected to have high transverse momenta since they carry a large fraction of the b-quark momentum due to the hard b-quark fragmentation. In addition, for the same large-R jet p_{T}, the decay products of the Higgs boson are more separated than those of W and Z bosons due to the higher Higgs boson mass, resulting in a slower degradation of the resolution in m^{calo} towards higher jet p_{T} for Higgs-jet.

The statistical correlation between the m^{calo} and m^{TA} measurements is modest (with linear correlation coefficient $\rho \sim 0.23$ for jets with $p_{\mathrm{T}} > 1$ TeV, as can be seen in Figure 1(b)), and therefore an uncertainty-weighted combination of the two variables, denoted as m^{comb}, is expected to result in an improved resolution. The m^{comb} resolution is found to be compatible with the m^{calo} resolution at Higgs-jet p_{T} below 600 GeV, with a resolution gain improving by up to 10% for a p_{T} of 2 TeV. Figure 2(a) shows the calibrated large-R jet mass distributions, m^{calo} and m^{TA}, including the muon correction discussed below, in the jet transverse momentum ranges of 350 GeV $< p_{\mathrm{T}} <$ 500 GeV and 1000 GeV $< p_{\mathrm{T}} <$ 1500 GeV.

The particle-level correction factors mentioned above do not account for semi-muonic decays, which occur in approximately 20% of all b-hadron decay chains. As the resulting neutrinos are not measured directly by the detector, only the muons are considered. The effect of these decays is corrected by finding muons within $\Delta R < 0.2$ of the b-tagged track jets and adding the four vector of these muons to that of the large-R calorimeter jet (while taking into account the muon energy loss in the calorimeter). If more than one muon is found within a track jet, only the muon closest to the track jet axis is considered. In case of m^{TA} only the jet calorimeter measurement of the jet p_{T} is corrected. The m^{calo} and m^{TA} mass distributions of the large-R Higgs jets are shown in Figure 2(b) before and after the muon correction in the 350 GeV $< p_{\mathrm{T}} <$ 500 GeV range. The mass resolution of Higgs-jets is clearly improved in both cases at low Higgs-jet p_{T}, while the improvement is not as pronounced at higher p_{T} as has been shown in Ref. [11].

Given the limited improvement obtained from combining the calorimeter-based jet mass definition m^{calo} with the track-assisted jet mass m^{TA}, the m^{calo} definition is used throughout the note. The muon correction is added on top.

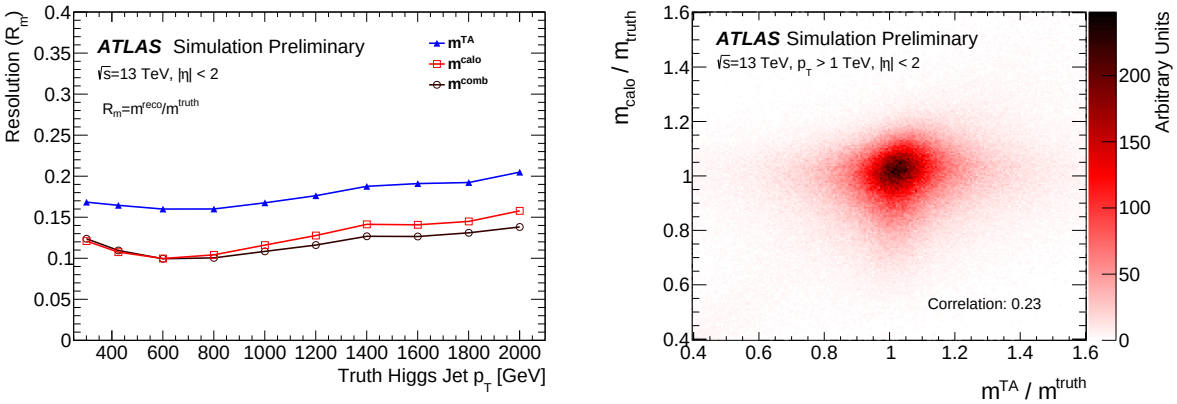

(a) (b)

Figure 1: (a) The resolution in the response of invariant mass of large-R Higgs-jets $R_m = \frac{m_{\text{reco}}}{m_{\text{truth}}}$ as a function of the transverse momentum p_{T} of the Higgs-jet for $|\eta| < 2$. The resolution is defined here as half the central 68% probability interval divided by the median of the jet mass response distribution. (b) The correlation between the responses in the m^{calo} and m^{TA} observables for large-R Higgs-jets with $p_{\text{T}} > 1$ TeV and within $|\eta| < 2$. The muon corrections described in the text are applied.

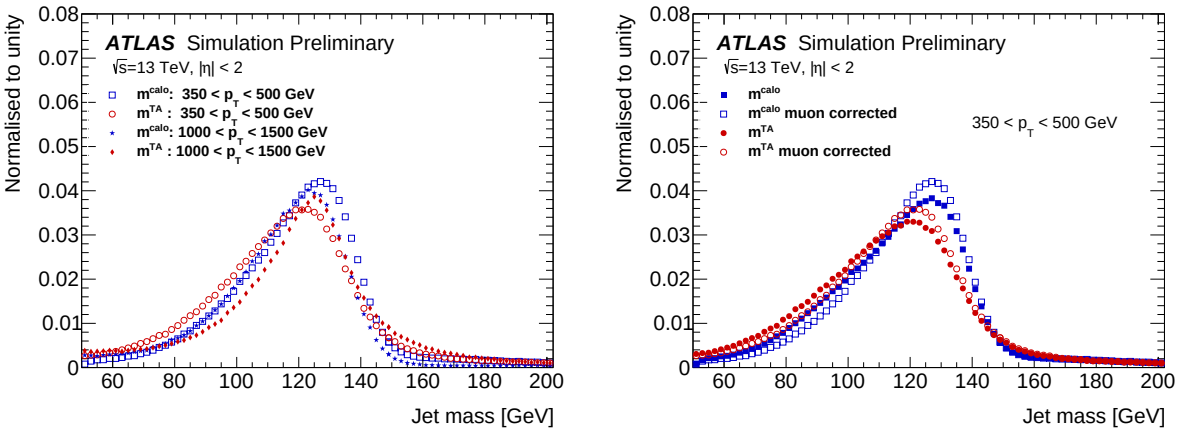

(a) (b)

Figure 2: (a) The calibrated large-R jet mass distributions, m^{calo} and m^{TA}, after the muon correction described in the text, are shown in the large-R jet transverse momentum ranges of 350 GeV $< p_{\text{T}} <$ 500 GeV and 1000 GeV $< p_{\text{T}} <$ 1500 GeV. (b) The calibrated large-R jet mass distributions, m^{calo} and m^{TA}, before and after the muon correction, are shown in the jet transverse momentum range of 350 GeV $< p_{\text{T}} <$ 500 GeV.

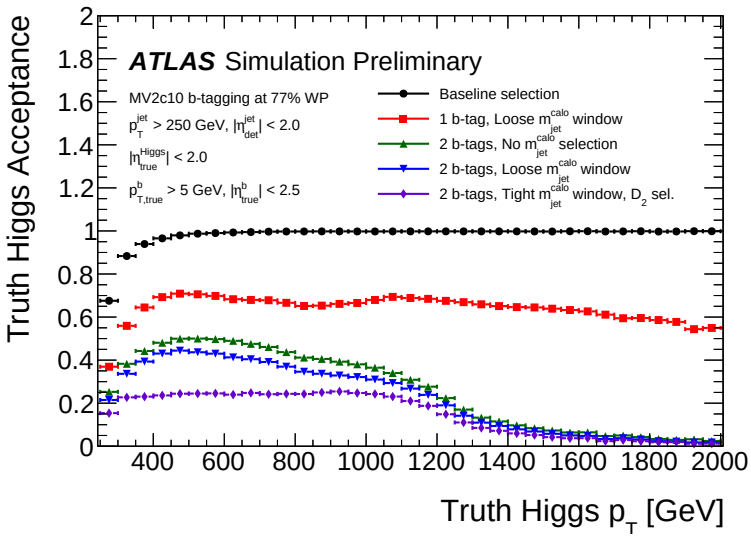

Figure 3: Truth Higgs boson acceptance, defined as the fraction of truth Higgs bosons with $|\eta| < 2.0$, and with b-hadrons from the Higgs boson decay with $p_{\mathrm{T}} > 5$ GeV and $|\eta| < 2.5$, that are associated to the reconstructed large-R jets after the baseline selection defined in Section 4. The effects of additional Higgs-jet tagging requirements are shown as additional curves.

5 Higgs-jet tagger

In this section, the Higgs-jet tagging procedure is described and its performance in terms of tagging efficiency and background rejection is discussed. The Higgs-jet tagging consists of the following steps:

- track jet b-tagging
- large-R jet mass window cut around the Higgs boson mass peak
- cut on large-R jet substructure variables

The first step in identifying boosted Higgs bosons is the large-R jet reconstruction. The acceptance of this reconstruction step, defined as the fraction of truth Higgs bosons with $p_{\mathrm{T}} > 250$ GeV, $|\eta| < 2.0$, and with b-hadrons from the Higgs boson decay with $p_{\mathrm{T}} > 5$ GeV and $|\eta| < 2.5$, that are reconstructed with the baseline large-R jet selection and labelled as a Higgs-jet (using the selection and labelling criteria defined in Section 4), is shown as a function of truth Higgs boson p_{T} in Figure 3. The angular separation between the decay products of the Higgs boson can be approximated by $\Delta R \approx \frac{2m_H}{p_{\mathrm{T}}}$, thus only for Higgs boson p_{T} values above 250 GeV its decay products will be collimated within $\Delta R \lesssim 1.0$, i.e. within a single large-R jet. This acceptance increases rapidly with Higgs boson p_{T}, reaching more than 95% for $p_{\mathrm{T}} > 400$ GeV.

The large-R jet p_{T} of signal and background samples differ. Therefore, for the performance studies and optimisations discussed in this note, the signal samples are summed together and reweighted to the jet p_{T} distribution of the multi-jet sample. The same procedure is applied to the hadronic $t\bar{t}$ samples. In the following subsections, the Higgs-jet tagging efficiency is defined as the number of Higgs-jets passing a given selection requirement divided by the total number of Higgs-jets passing the baseline selection

defined in Section 4. The background rejection is defined as the inverse of the efficiency for a background jet to pass the requirement.

5.1 Track jet *b*-tagging performance

The *b*-tagging for large-*R* jets is performed by means of the ghost associated track jets. The track jets are always ordered by p_{T}, and only the leading two track jets (if they exist) are used for double and asymmetric *b*-tagging. For single *b*-tagging benchmarks only one track jet associated to the large-*R* jet is required. A track jet is considered to have passed the *b*-tagging requirement if the track jet's MV2c10 *b*-tagging weight, $w_{b-\mathrm{tag}}$, is larger than a threshold value, w_X. The value of w_X can be scanned to examine the background rejection as a function of Higgs-jet efficiency for different *b*-tagging requirements.

Several different *b*-tagging requirements on the track jets are examined:

- *Double b-tagging*: the two leading p_{T} track jets must both pass the same *b*-tagging requirement of having $w_{b-\mathrm{tag}} > w_X$.
- *Asymmetric (Asymm.) b-tagging*: Of the two leading p_{T} track jets, the track jet with the largest *b*-tagging weight must pass the fixed 60%, 70%, 77% or 85% *b*-tagging working point threshold, e.g. $w_{b-\mathrm{tag}} > w_{70\%}$, while the *b*-tagging requirement of the other jet is varied.
- *Leading subjet single b-tagging*: only the leading p_{T} track jet must pass the *b*-tagging requirement of having $w_{b-\mathrm{tag}} > w_X$.
- *Single b-tagging*: at least one of the two leading p_{T} track jets must pass the *b*-tagging requirement of having $w_{b-\mathrm{tag}} > w_X$.

The Higgs-jet efficiency versus the inclusive multi-jet rejection can be found in Figure 4(a), where the performance of all benchmarks is shown. The double and asymmetric *b*-tagging curves do not reach a Higgs-jet efficiency of 100% due to a requirement of at least two track jets needed for double *b*-tagging (the baseline selection requires only one track jet) and, in the case of asymmetric *b*-tagging, due also to the fixed *b*-tagging working point requirement on one of the track jets. The background rejection of single *b*-tagging is larger than that of the leading subjet single *b*-tagging in general and especially for high signal efficiencies. For high Higgs-jet efficiencies, above $\sim$ 75%, a high double *b*-tagging efficiency is only possible at the expense of a high tagging efficiency for individual light-flavour jets, and the single *b*-tagging approach tends to have a better multi-jet rejection than the double *b*-tagging. For lower Higgs-jet efficiency the double *b*-tagging approach provides a significantly higher multi-jet rejection. Finally, the asymmetric *b*-tagging option is seen to capture much of the benefits of double *b*-tagging in the low Higgs-jet efficiency regime, while being significantly better than both single and double *b*-tagging in the high Higgs-jet efficiency regime except at very high efficiencies above $\sim$ 90%, where the single *b*-tagging approach shows the best performance.

While Figure 4(a) includes all large-*R* jets with $p_{\mathrm{T}} > 250$ GeV, Figure 4(b) shows the performance of *b*-tagging requirements for large-*R* jet p_{T} above 1 TeV. In this p_{T} regime, the single *b*-tagging approach has the best performance already at signal efficiencies above $\sim$ 55%, while the double and asymmetric *b*-tagging options have a similar performance below $\sim$ 25%. In the signal efficiency range between $\sim$ 25% and $\sim$ 55%, the asymmetric *b*-tagging approach has the best background rejection.

Another common background to boosted Higgs boson searches are boosted hadronic top-quark decays. The inclusive hadronic top jet rejection versus the Higgs-jet efficiency can be found in Figure 4(c), where

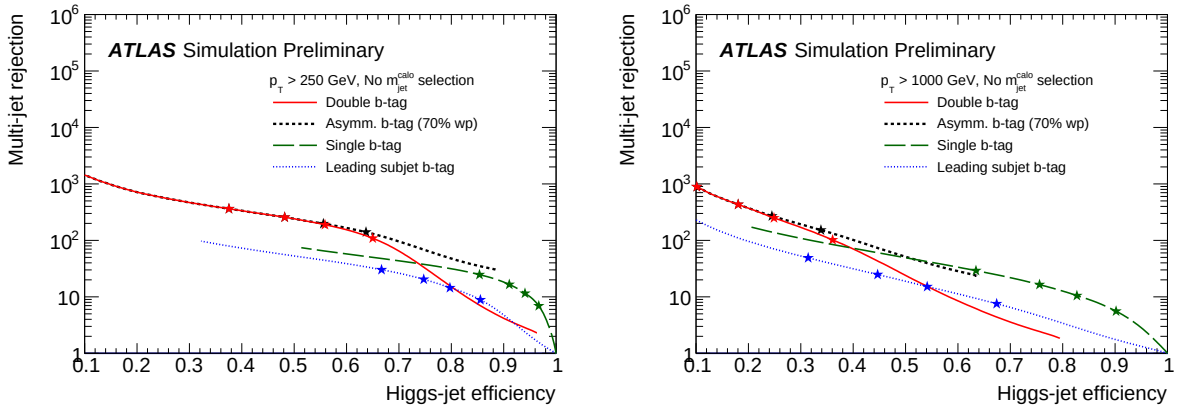

(a)

(b)

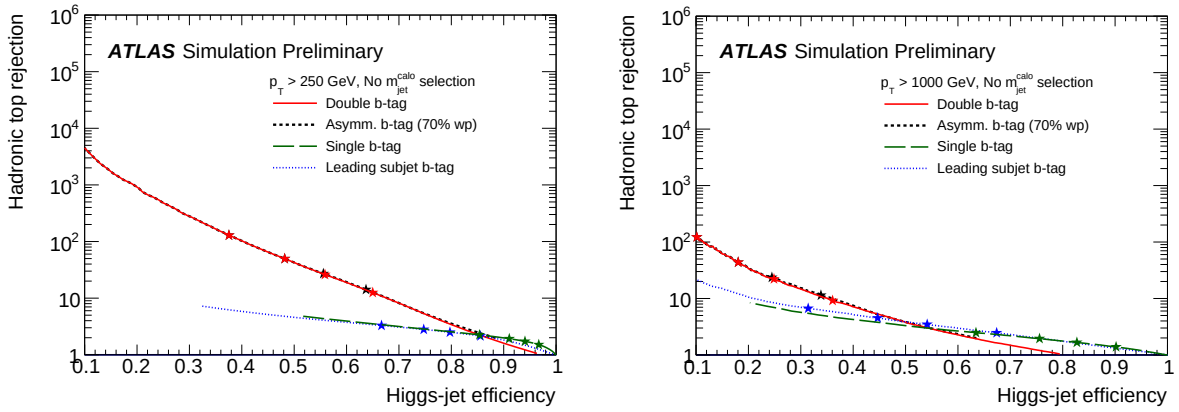

(c)

(d)

Figure 4: (a) The rejection of inclusive multi-jets versus Higgs-jet efficiency using large-R jets with $p_{\mathrm{T}} > 250$ GeV, for various b-tagging requirements. (b) Same as (a) but using large-R jets with $p_{\mathrm{T}} > 1000$ GeV. (c) Hadronic top background rejection versus Higgs-jet efficiency using all large-R jets with $p_{\mathrm{T}} > 250$ GeV, for various b-tagging requirements. (d) Same as (c) but using large-R jets with $p_{\mathrm{T}} > 1000$ GeV. The stars correspond to the 60%, 70%, 77% and 85% b-tagging WPs (from left to right).

the performance of double b-tagging, single b-tagging and asymmetric b-tagging is shown. Double and asymmetric b-tagging perform similarly and both provide significantly better rejection than single b-tagging with no significant loss in Higgs-jet efficiency. Only for very high Higgs-jet efficiencies, above $\sim 85\%$, the single b-tagging approach has a higher background rejection than the double and asymmetric b-tagging options. Figure 4(d) shows the hadronic top jet rejection for large-R jet p_{T} above 1 TeV. A similar behaviour as for the multi-jet rejection is observed: the single b-tagging approach has the best performance above 55% signal efficiency, for lower signal efficiencies the double and asymmetric b-tagging show a better background rejection.

5.2 Mass window and substructure requirements

The groomed and muon corrected calorimeter reconstructed mass m^{calo} is an important component in tagging boson jets [11]. A mass window requirement, selecting a range of masses around the Higgs boson mass, is applied. The 93–134 GeV and 76–146 GeV intervals are used as the smallest intervals containing approximately 68% ("tight mass window cut") and 90% ("loose mass window cut") of the groomed Higgs-jet mass distributions, respectively. The mass intervals are derived for the Higgs-jet sample integrated over the full p_{T} spectrum.

Figure 5 shows the Higgs tagging performance for the same b-tagging benchmarks as in Figure 4 but adding the loose and tight mass window requirements. The conclusions are similar to the ones described in the previous section.

In addition to the heavy flavour content of the large-R jet, and the jet mass, the internal structure of the jet can be used to discriminate Higgs-jets from multi-jet production and hadronic top decays. There are a large number of substructure variables that capture features of a jet's internal structure. $D_2^{(\beta=1)}$ [39, 40] is used in this analysis, defined as a ratio of the two and three point energy correlation functions, which are based on the energies and pair-wise angular distances of particles within a jet. This variable was optimised to separate between one-prong and two-prong decays. A detailed description can be found in Ref. [32]. Previous studies [9, 32, 41] have shown that this variable is one of the most sensitive for this topology; in addition, calibration as well as resolution and scale uncertainties have been derived for this variable. A p_{T} dependent selection identical to the one of Ref. [11] is applied here.

5.3 Systematic uncertainties of the Higgs-jet tagger performance

To estimate the experimental systematic uncertainties of the Higgs-jet tagger performance, the uncertainties on the Higgs-jet tagger inputs are propagated through the tagger selection. More specifically, the b-tagging efficiency and the jet mass, p_{T}, and $D_2^{(\beta=1)}$ scale and resolutions are varied within their uncertainties [38]. These input uncertainties lead to changes in the efficiency or acceptance or both of the Higgs-jet tagger selection, and thus provide an estimate of the systematics uncertainties of the Higgs-jet efficiency and background rejection.

Figures 6, 7 and 8 show the Higgs-jet tagging efficiency and background rejection, including the effect of various systematic uncertainties. The largest uncertainty is the b-tagging uncertainty, especially for the double b-tagging working point; the jet related systematics become larger at very high jet p_{T}. Figure 9 shows the Higgs-jet tagging efficiency and background rejection for all benchmarks defined in 5.1. The total uncertainty is the sum in quadrature of the statistical and systematic uncertainties.

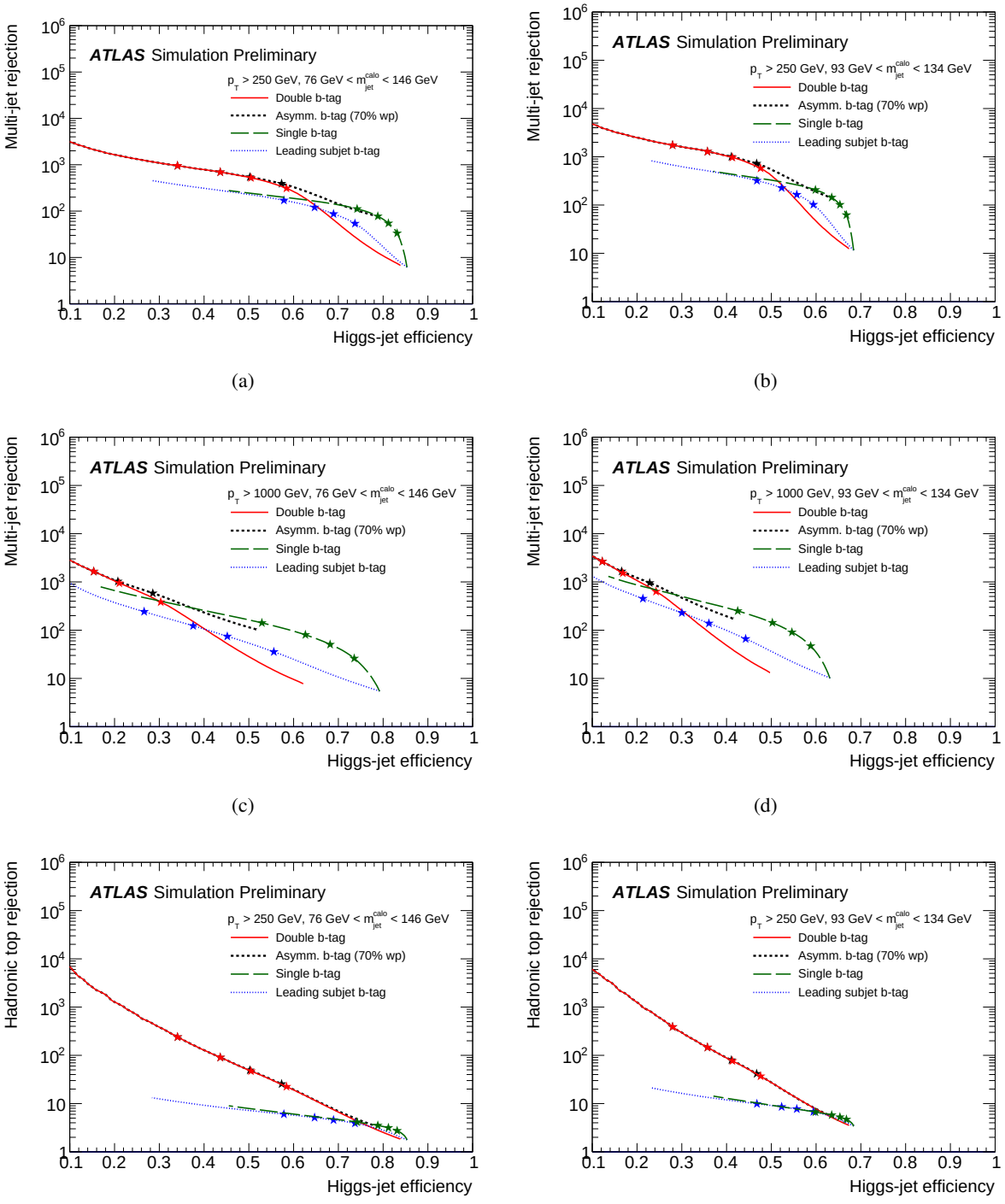

Figure 5: Top: The rejection of inclusive multi-jet background versus Higgs-jet efficiency using large-R jets with $p_{\mathrm{T}} > 250$ GeV for various b-tagging requirements using loose (a) and tight (b) mass window cuts. Middle: Same as above, but using all large-R jets with $p_{\mathrm{T}} > 1000$ GeV. Bottom: Hadronic top background rejection versus Higgs-jet efficiency using all large-R jets with $p_{\mathrm{T}} > 250$ GeV for various b-tagging requirements using loose (e) and tight (f) mass window cuts. The stars correspond to the 60%, 70%, 77% and 85% b-tagging WPs (from left to right).

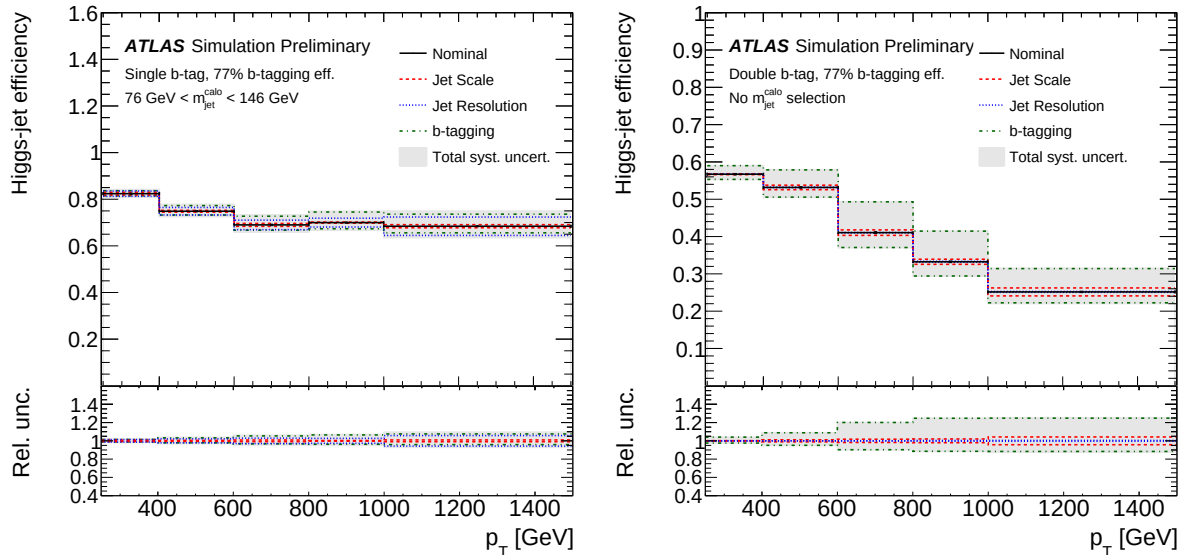

(a)

(b)

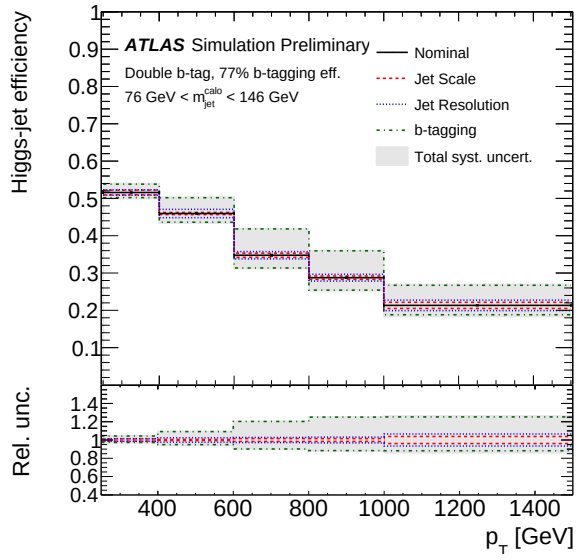

(c)

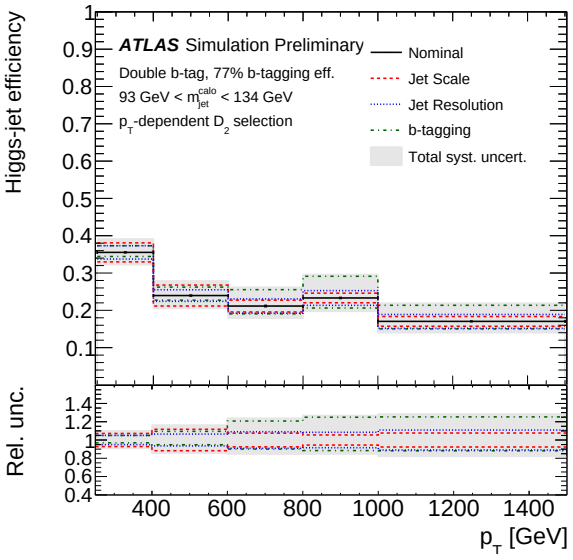

(d)

Figure 6: Higgs-jet signal efficiency as a function of the p_{T} of large-R jets using the 77% b-tagging WP, and requiring various Higgs-jet mass window cuts and b-tagging requirements: (a) at least one associated b-tagged track jet and a loose mass window cut, (b) two associated b-tagged track jets and no mass window cut, (c) two associated b-tagged track jets and a loose mass window cut, (d) two associated b-tagged track jets, a tight mass window cut and a cut on $D_2^{(\beta=1)}$.

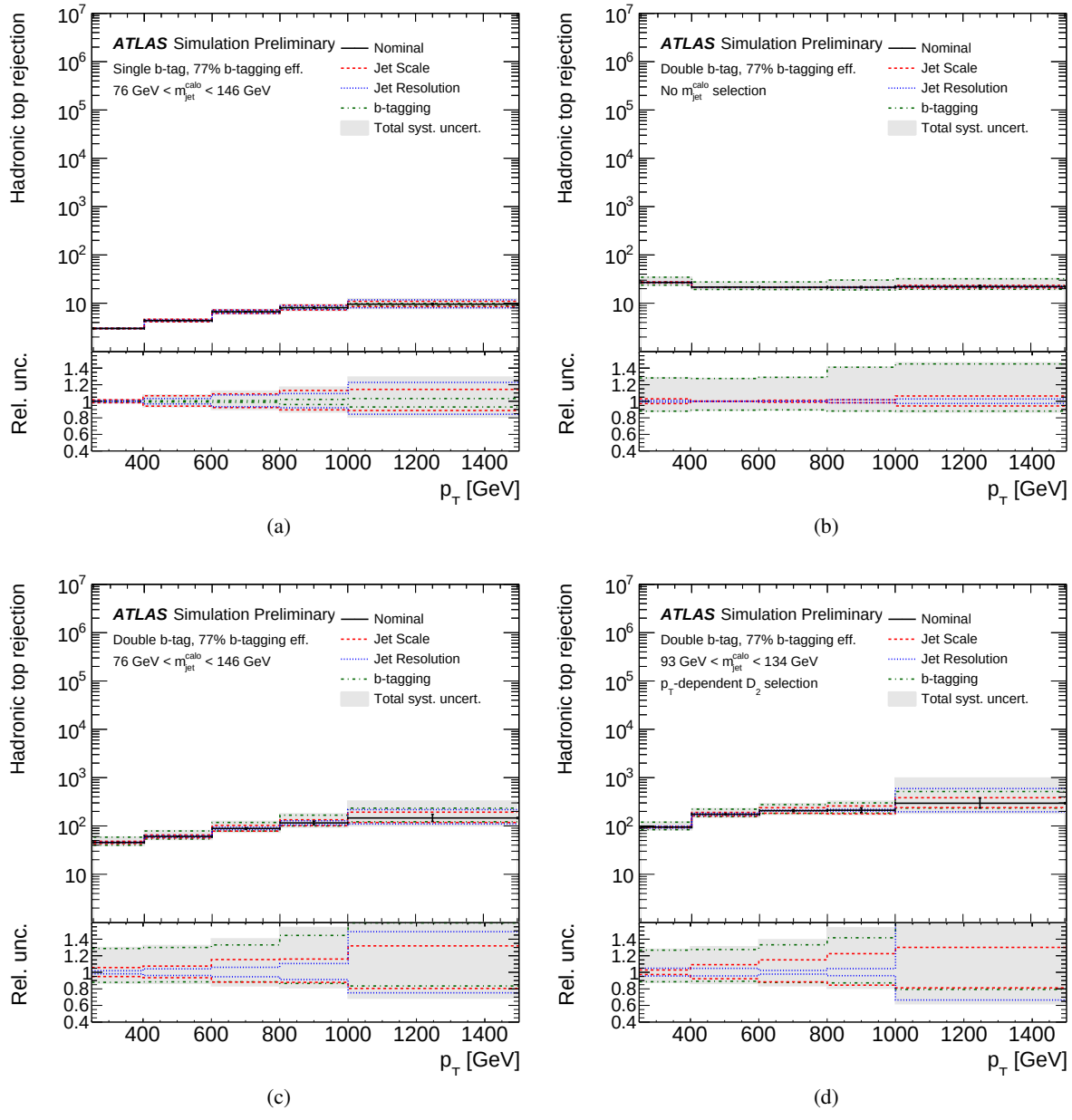

Figure 7: Hadronic top background rejection as a function of the p_{T} of large-R jets using the 77% b-tagging WP, and requiring various Higgs-jet mass window cuts and b-tagging requirements: (a) at least one associated b-tagged track jet and a loose mass window cut, (b) two associated b-tagged track jets and no mass window cut, (c) two associated b-tagged track jets and a loose mass window cut, (d) two associated b-tagged track jets, a tight mass window cut and a cut on $D_2^{(\beta=1)}$.

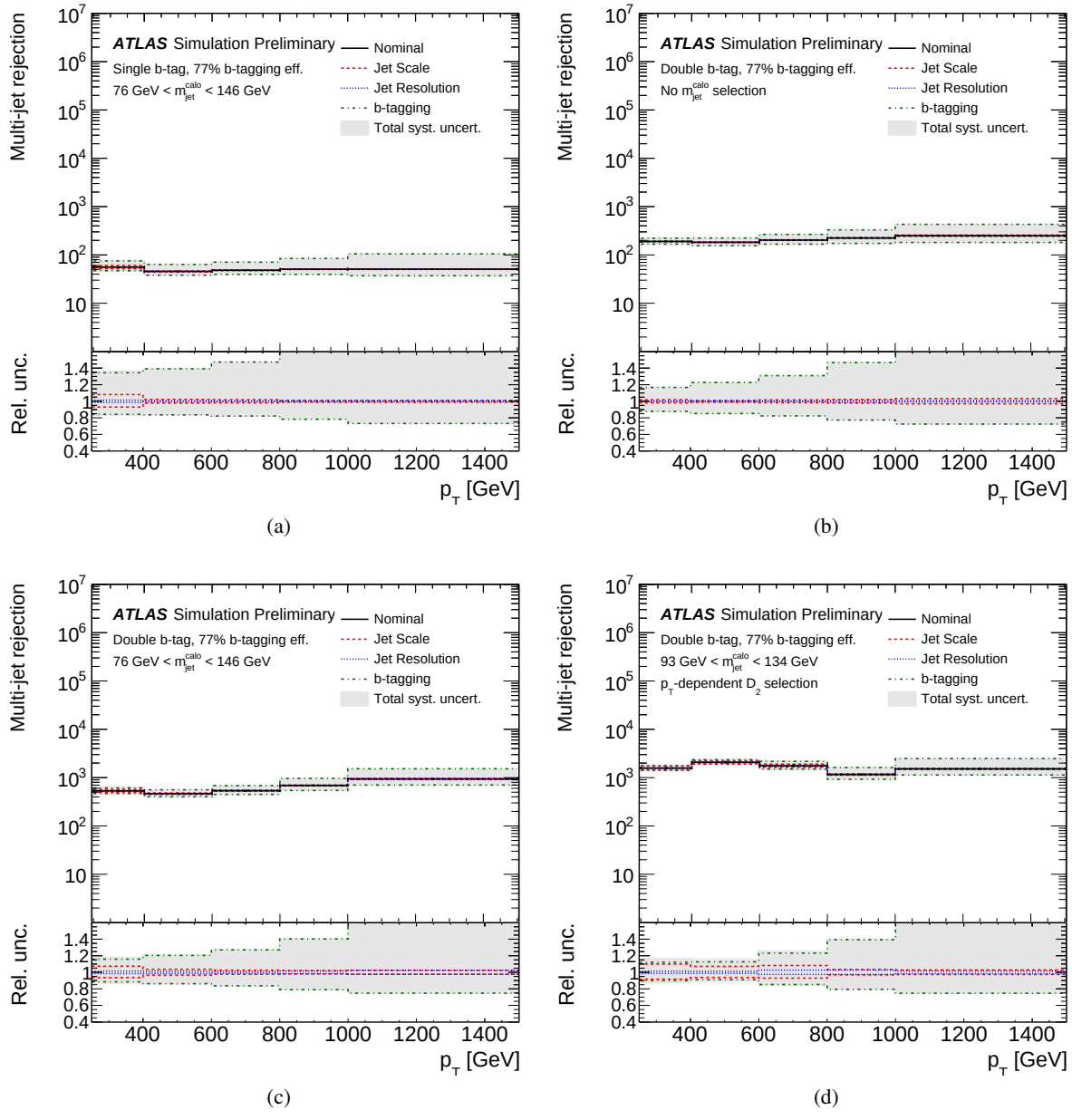

Figure 8: Multi-jet background rejection as a function of the p_{T} of large-R jets using the 77% b-tagging WP, and requiring various Higgs-jet mass window cuts and b-tagging requirements: (a) at least one associated b-tagged track jet and a loose mass window cut, (b) two associated b-tagged track jets and no mass window cut, (c) two associated b-tagged track jets and a loose mass window cut, (d) two associated b-tagged track jets, a tight mass window cut and a cut on $D_2^{(\beta=1)}$.

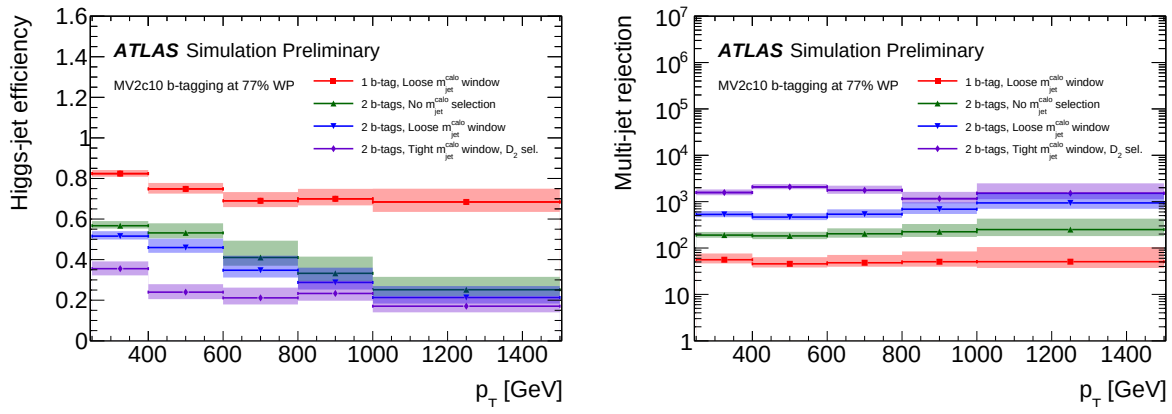

(a)

(b)

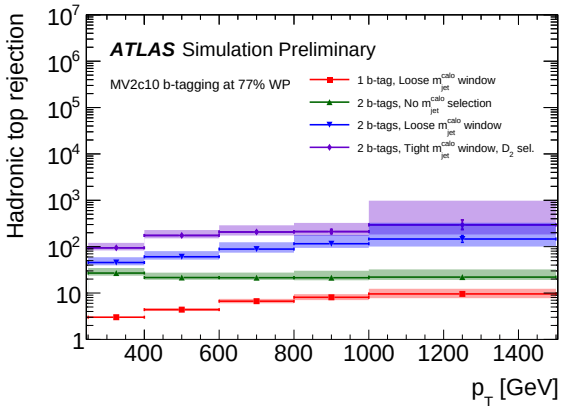

(c)

Figure 9: (a) Higgs-jet signal efficiency, (b) Multi-jet background rejection and (c) Hadronic top background rejection as a function of the p_{T} of large-R jets with one or two associated b-tagged track jets, using the 77% b-tagging WP, and requiring various Higgs-jet mass window cuts and a cut on $D_2^{(\beta=1)}$.

6 Validation in $g \to b\bar{b}$

In order to ensure the accurate modelling of a Higgs tagger in simulation, it is vital to compare the tagger's performance in MC simulation and data. While it is difficult to find a pure sample of $b\bar{b}$ decays from a boosted colour singlet resonance, it is possible to identify gluon $g \to b\bar{b}$ splitting in QCD multi-jet events, where $b\bar{b}$ production is dominated by this process. As such, a pure sample of two close-by b-jets is found by requiring that two small-R track jets are present in a large-R jet with a muon associated to at least one of the track jets and both track jets pass the b-tagging requirement. This sample is then used to cross-check the performance of b-tagging and evaluate the modelling of jet substructure variables in data by the MC. Such a study was carried out using the 8 TeV Run 1 data [42] and is repeated here using the 2015 13 TeV Run 2 data.

One difficulty with studying this sample is the fact that the fraction of jets initiated by different quark flavours is typically not well modelled by the MC simulation. This causes difficulties because the different jet flavours have vastly different efficiencies to pass the b-tagging requirements (by construction). Therefore, it is necessary to first correct the flavour fractions before b-tagging so that the MC modelling of the b-tagging efficiency can be isolated and properly studied. The flavour fractions are corrected by simultaneously fitting the impact parameter significance distributions of the tracks in the two close-by jets.

6.1 Event selection

The triggers used to collect the data were prescaled; therefore, MC samples for each trigger jet p_{T} bin are normalised to the luminosity calculated separately for each trigger. The leading p_{T} $R = 0.4$ offline anti-k_t jet is called the triggering jet, j_{trigger}. No explicit matching is made of these jets to the trigger system jet that fired the trigger.

Following the procedure described in Section 5, selected events are required to have at least one large-R jet with $p_{\mathrm{T}} > 250$ GeV and $|\eta| < 2.0$. Additionally this jet must have at least two ghost associated $R = 0.2$ track jets. This topology of a high-p_{T} large-R jet with at least two matched track jets focuses on identifying $g \to b\bar{b}$ events, where the large-R jet is the proxy for the gluon while the track jets are proxies for the b quarks. In order to enrich the event sample in jets containing b-hadrons, it is required that at least one of the ghost associated track jets be matched to a muon. The highest p_{T} track jet matched to a muon is called the muon-tagged jet, j_{μ}^{trk}. The leading p_{T} jet among the remaining track jets ghost-associated to the large-R jet is called the non-muon jet, $j_{\mathrm{non}-\mu}^{\mathrm{trk}}$. The highest p_{T} large-R jet passing these criteria is selected as the gluon jet candidate. Furthermore, the event must satisfy $\Delta R(j_{\mathrm{trigger}}, j_{\mu}^{\mathrm{trk}}) > 1.5$. This requirement ensures that the triggering jet and the gluon candidate jet are well separated, and thus that the trigger requirement is independent of the gluon candidate selection.

As the trigger prescaling shapes the offline jet p_{T} spectrum, the spectrum of j_{trigger} in MC simulation is weighted to match the observed spectrum in data. Additionally, a difference in the η spectrum of j_{trigger} between data and MC simulation is observed, so a two-dimensional reweighting in p_{T} and η is applied to the MC simulation.

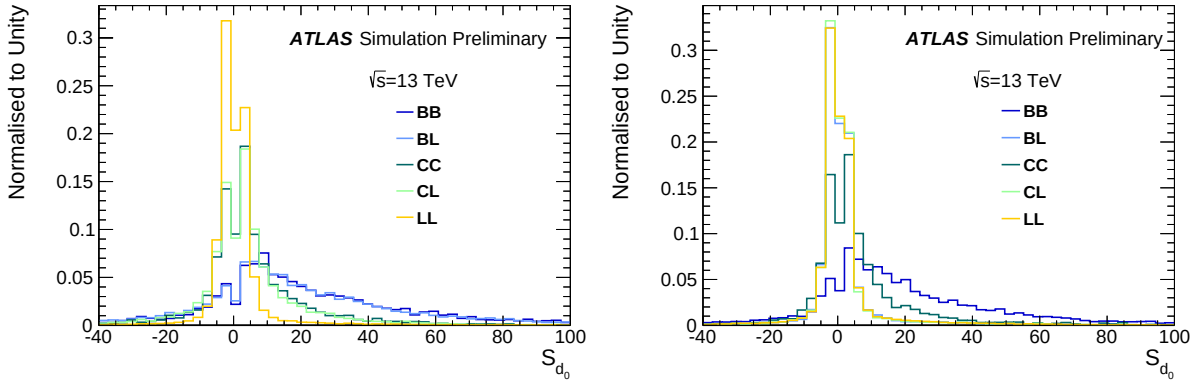

Figure 10: S_{d_0} distributions for the muon (left) and non-muon jets (right). The double flavour labels denote the flavour of the jet pair, with the muon jet given first.

6.2 Flavour fraction corrections

In order to study the performance of the Higgs tagging algorithm and modelling of jet properties, discrepancies arising from differences between data and MC simulation in the flavour composition of the large-R jet must be factorised out of the comparison. Therefore, the flavour fractions of the sample are determined directly from the data by fitting a distribution sensitive to the relative composition of the different flavours of jets before using jet flavour tagging. The following describes briefly the flavour fraction determination; more details can be found in Ref. [42].

Each large-R jet effectively carries two flavours, that of j_{μ}^{trk} and $j_{\text{non}-\mu}^{\text{trk}}$, leaving 9 possible flavour combinations of the large-R jet (if each track jet can be b, c, and light). In order to extract the flavour fraction of each of these components, from each track jet's three highest p_{T} tracks the track with the highest transverse impact parameter significance $|S_{d_0}|$ is selected. Here, the S_{d_0} of a track is defined as:

$$S_{d_0} = \frac{d_0}{\sigma(d_0)} s_j, \tag{1}$$

where d_0 is the track transverse impact parameter with respect to the primary vertex, $\sigma(d_0)$ is the uncertainty on the d_0 measurement, and s_j is the sign of d_0 with respect to the jet axis, depending on whether the track crosses the jet axis in front of or behind the primary vertex. The track transverse impact parameter distributions in MC simulation are smeared as a function of track η and p_{T} using Gaussian functions derived in 2015 minimum bias data [43]. This procedure is needed to account for missing material in the simulation, especially in proximity of the new IBL pixel layer [44], and for residual misalignment effects, that are not considered in the simulation . A binned likelihood fit is performed to the S_{d_0} distribution.

While in principle a 2-dimensional fit to $S_{d_0}(j_{\mu}^{\text{trk}})$ vs. $S_{d_0}(j_{\text{non}-\mu}^{\text{trk}})$ should be performed, the S_{d_0} values of the two jets are observed to be uncorrelated and thus the 1-dimensional distributions of each jet's S_{d_0} can be fit simultaneously using the same flavour fraction parameters. Furthermore, the flavour combinations of $(j_{\mu}^{\text{trk}}, j_{\text{non}-\mu}^{\text{trk}}) = \{(b,\ c),\ (c,\ b),\ (l,\ c),\ (l,\ b)\}$ are predicted to be less than 1% of the total. As such they are merged with other flavour fraction components which have the closest shape. Thus a total of 5 flavour fraction parameters are used, $(j_{\mu}^{\text{trk}}, j_{\text{non}-\mu}^{\text{trk}}) = \{(b,\ b),\ (b,\ l),\ (c,\ c),\ (c,\ l),\ (l,\ l)\}$. Figure 10 shows the templates inclusive in p_{T}.

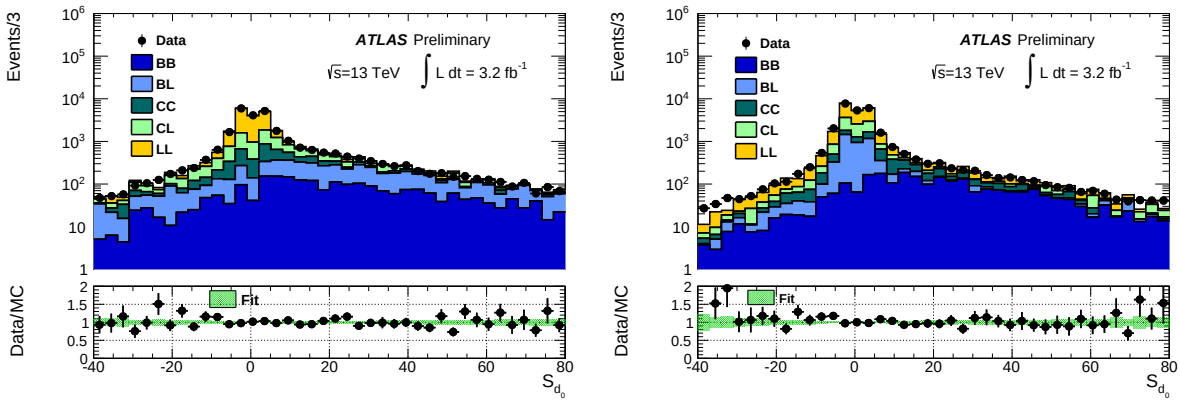

Figure 11: S_{d_0} distributions of the muon and non-muon jet in bin 100 GeV $< p_{\mathrm{T}}(j_{\mu}^{\mathrm{trk}}) <$ 200 GeV and $p_{\mathrm{T}}(j_{\mathrm{non}-\mu}^{\mathrm{trk}}) >$ 80 GeV. The lower panels show the ratios of the distributions measured in data to their predictions, also indicating the uncertainty on the predictions resulting from the template fitting procedure.

As the flavour fractions vary with p_{T}, the flavour fraction fits are performed in bins of p_{T} of the two track jets. The following jet p_{T} bins are used: j_{μ}^{trk} p_{T}-bins = $\{(0-100), (100-200), > 200\}$ GeV and $j_{\mathrm{non}-\mu}^{\mathrm{trk}}$ p_{T} bins=$\{(0-20), (20-50), (50-80), > 80\}$ GeV. The results of the flavour fraction fit to the S_{d_0} distributions of j_{μ}^{trk} and $j_{\mathrm{non}-\mu}^{\mathrm{trk}}$ can be seen in Figure 11.

After correcting for observed flavour-pair fractions the agreement between data and MC simulation is evaluated in the selected event sample before and after b-tagging is applied to the small-R track jets. To b-tag the small-R track jets the 70% efficiency working point is used.

6.3 b-tagging results

As the flavour fractions are corrected in the MC simulation, deviations between the data and predictions after the b-tagging can be attributed to a difference between data and MC simulation in the dependence of the b-tagging performance on the event topology, beyond the scale factor derived for inclusive track jets. Figure 12 shows the p_{T} spectrum of the j_{μ}^{trk} and $j_{\mathrm{non}-\mu}^{\mathrm{trk}}$ before and after b-tagging.

The double b-tagging rate,

$$\text{double b-tagging rate} = \frac{\text{all selected large-}R\text{ jets with 2 b-tags}}{\text{all selected large-}R\text{ jets}}, \tag{2}$$

as a function of the large-R jet p_{T} is shown in Figure 13, for all jet satisfying the selection requirements of the analysis. Data and MC simulation agree reasonably well.

6.4 Jet substructure results

As the Higgs tagger will make use of the large-R jet kinematics like p_{T}, and substructure variables like mass or $D_2^{(\beta=1)}$, it is important to ensure these variables are well modelled by MC simulation. The distribution of kinematic and substructure variables can be found in Figure 14, for double b-tagged jets after the flavour fit correction. The uncertainty bands include jet energy, mass and $D_2^{(\beta=1)}$ scale and resolution

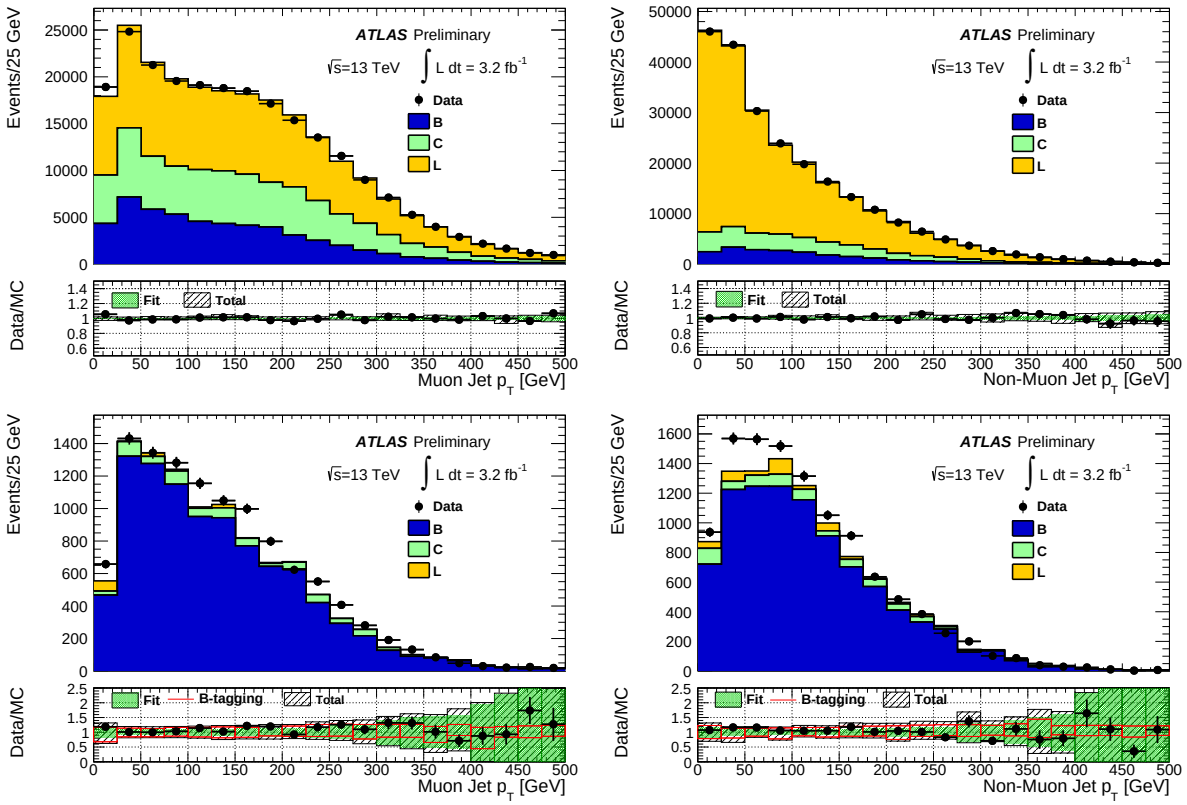

Figure 12: p_{T} of the j_{μ}^{trk} (left) and $j_{\mathrm{non}-\mu}^{\mathrm{trk}}$ (right) before (top) and after (bottom) b-tagging. b-tagging scale factors and the flavour fraction correction have been applied. The lower panels show the ratios of the distributions measured in data to their predictions, also indicating the uncertainty on the predictions resulting from the template fitting procedure, from the limited simulated sample sizes, jet energy scale and resolution uncertainties, b-tagging systematics (bottom plots only), and their combination.

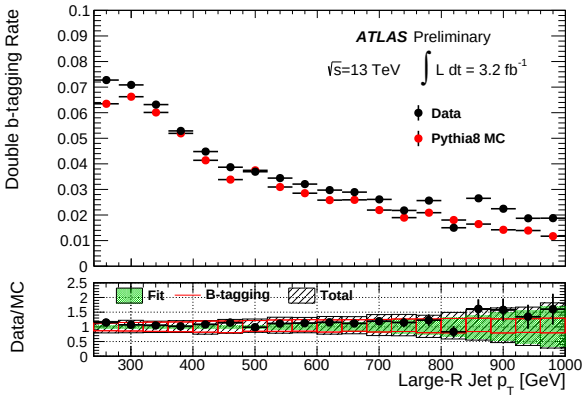

Figure 13: Comparison between data and MC simulation of the double b-tagging rate as a function of the large-R jet p_{T}. The lower panel shows the ratio of the distribution measured in data to its prediction, also indicating the uncertainty on the predictions resulting from the template fitting procedure, from the limited simulated sample sizes, b-tagging systematics, and their combination.

uncertainties, b-tagging systematics, the fit uncertainties as well the uncertainty from the limited simulated sample sizes. The dominant uncertainties for double b-tagged jets are the fit uncertainty and the b-tagging systematics. Even if a trend is visible in the jet mass and $D_2^{(\beta=1)}$ distributions, the jet properties are adequately modelled, within the uncertainties.

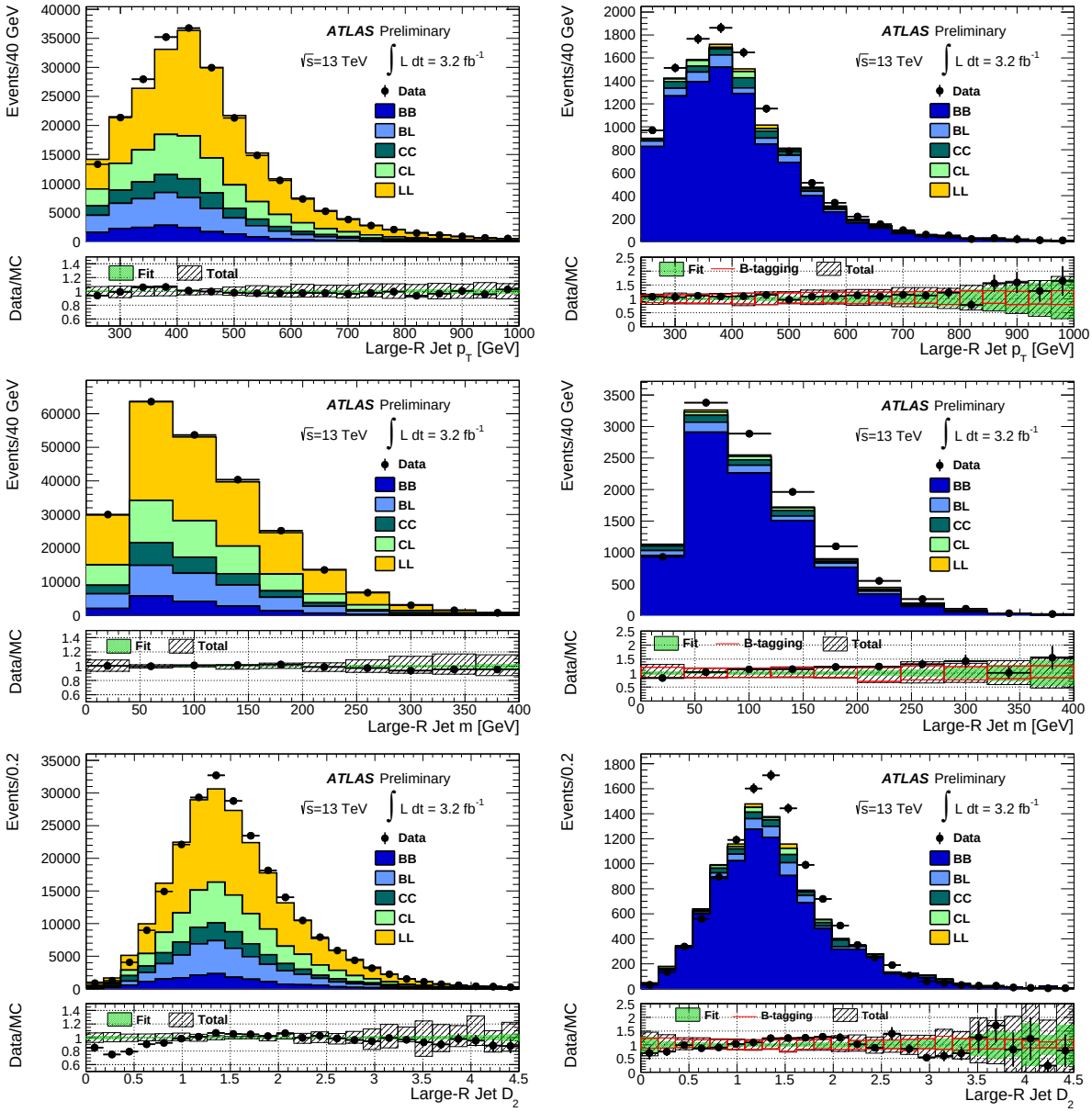

Figure 14: Distributions of large-R jet p_{T} (top), mass (middle) and $D_2^{(\beta=1)}$ (bottom) before (left) and after (right) b-tagging. The lower panels show the ratios of the distributions measured in data to their predictions, also indicating the uncertainty on the predictions resulting from the template fitting procedure, from the limited simulated sample sizes, jet energy, mass and $D_2^{(\beta=1)}$ scale and resolution uncertainties, b-tagging systematics and their combination.

7 Conclusions

The performance of the identification of high-p_{T} $H \to b\bar{b}$ decays in the ATLAS experiment has been re-optimised and re-evaluated using updated b-tagging criteria and large-R jet mass reconstruction. As an example, for the 77% b-tagging working point and jets with $p_{\mathrm{T}} > 1$ TeV, in a double-tagging scenario using a loose mass window cut (tight mass window cut), Higgs-jet signal efficiencies of 22% (17%) are obtained; for these same criteria, hadronic top quark jet rejections of 190 (300) and multijet rejections of about 900 (1200) are obtained. The performance in the regime with two close-by b jets, as appropriate for the Higgs boson decays to $b\bar{b}$, has been studied in a sample of $g \to b\bar{b}$ candidates. It is found that the b-jet tagging efficiency is reasonably well modelled in simulated events. The distributions of the large-R jet mass and p_{T}, as well as that of the $D_2^{(\beta=1)}$ jet substructure variable has been studied, and is found to be reasonably well modelled in simulated events, with small shape differences.

References

[1] ATLAS Collaboration, *The ATLAS Experiment at the CERN Large Hadron Collider*, JINST **3** (2008) S08003.

[2] L. Randall and R. Sundrum, *A Large Mass Hierarchy from a Small Extra Dimension*, Phys. Rev. Lett. **83** (1999) 3370, arXiv: hep-ph/9905221.

[3] K. Matchev and K. Thomas, *Higgs and Z-boson signatures of supersymmetry*, Phys. Rev. **D 62** (2000) 077702.

[4] G. Branco et al., *Theory and phenomenology of two-Higgs-doublet models*, Phys. Rept. **516** (2012) 1, arXiv: 1106.0034 [hep-ex].

[5] ATLAS Collaboration, *Observation of a new particle in the search for the Standard Model Higgs boson with the ATLAS detector at the LHC*, Physics Letters B **716** (1 2012) 1, arXiv: 1207.7214 [hep-ex].

[6] CMS Collaboration, *Observation of a new boson at a mass of 125 GeV with the CMS experiment at the LHC*, Physics Letters B **716** (1 2012) 30, arXiv: 1207.7235 [hep-ex].

[7] B. Cooper et al., *Boosted $hh \to b\bar{b}b\bar{b}$: A new topology in searches for TeV-scale resonances at the LHC*, Phys. Rev. D **88** (2013) 114005, arXiv: 1307.0407 [hep-ex].

[8] J. M. Butterworth et al., *Jet substructure as a new Higgs search channel at the LHC*, Phys.Rev.Lett. **100** (2008) 242001, arXiv: 0802.2470 [hep-ph].

[9] ATLAS Collaboration, *Performance of Boosted W Boson Identification with the ATLAS Detector*, ATL-PHYS-PUB-2014-004, 2014, URL: https://atlas.web.cern.ch/Atlas/GROUPS/PHYSICS/PUBNOTES/ATL-PHYS-PUB-2014-004/.

[10] ATLAS Collaboration, *Flavor Tagging with Track-Jets in Boosted Topologies with the ATLAS Detector*, ATL-PHYS-PUB-2014-013, 2014, URL: https://atlas.web.cern.ch/Atlas/GROUPS/PHYSICS/PUBNOTES/ATL-PHYS-PUB-2014-013.

[11] ATLAS Collaboration, *Expected Performance of Boosted Higgs ($\to b\bar{b}$) Boson Identification with the ATLAS Detector at $\sqrt{s} = 13$ TeV*, ATL-PHYS-PUB-2015-035, 2015, URL: http://cdsweb.cern.ch/record/2042155.

[12] ATLAS Collaboration, *Performance of the ATLAS Trigger System in 2010*, Eur. Phys. J. C **72** (2012) 1849, arXiv: 1110.1530 [hep-ex].

[13] ATLAS Collaboration, *2015 start-up trigger menu and initial performance assessment of the ATLAS trigger using Run-2 data*, ATL-DAQ-PUB-2016-001, 2016, URL: https://cds.cern.ch/record/2136007/.

[14] ATLAS Collaboration, *Improved luminosity determination in pp collisions at $\sqrt{s} = 7$ TeV using the ATLAS detector at the LHC*, Eur. Phys. J. C **73** (2013) 2518, arXiv: 1302.4393 [hep-ex].

[15] ATLAS Collaboration, *Luminosity determination in pp collisions at $\sqrt{s} = 8$ TeV using the ATLAS detector at the LHC*, to be submitted to Eur. Phys. J. C (2015).

[16] M. Cacciari, G. P. Salam and G. Soyez, *The anti-k_t jet clustering algorithm*, JHEP **04** (2008) 063, arXiv: 0802.1189 [hep-ph].

[17] J. Alwall et al., *The automated computation of tree-level and next-to-leading order differential cross sections, and their matching to parton shower simulations*, JHEP **07** (2014) 079, arXiv: 1405.0301.

[18] T. Sjostrand, S. Mrenna and P. Z. Skands, *A Brief Introduction to PYTHIA 8.1*, Comput. Phys. Commun. **178** (2008) 852, arXiv: 0710.3820 [hep-ph].

[19] R. D. Ball et al., *Parton distributions with LHC data*, Nucl. Phys. **B867** (2013) 244, arXiv: 1207.1303 [hep-ph].

[20] ATLAS Collaboration, *ATLAS Pythia 8 tunes to 7 TeV data*, ATL-PHYS-PUB-2014-021, 2014, URL: http://cdsweb.cern.ch/record/1966419.

[21] P. Nason, *A New Method for Combining NLO QCD with Shower Monte Carlo Algorithms*, JHEP **11** (2004) 040, arXiv: hep-ph/0409146 [hep-ph].

[22] S. Frixione, P. Nason and C. Oleari, *Matching NLO QCD computations with Parton Shower simulations: the POWHEG method*, JHEP **11** (2007) 070, arXiv: 0709.2092 [hep-ph].

[23] T. Sjostrand, S. Mrenna and P. Skands, *PYTHIA 6.4 Physics and Manual*, JHEP **0605** (2006) 026, arXiv: 0603175 [hep-ph].

[24] P. Z. Skands, *Tuning Monte Carlo generators: The Perugia tunes*, Phys. Rev. **D 82** (2010) 074018, arXiv: 1005.3457 [hep-ph].

[25] D.J. Lange, *The EvtGen particle decay simulation package*, Nucl. Instr. Meth. **A462** (2001) 152.

[26] ATLAS Collaboration, *Topological cell clustering in the ATLAS calorimeters and its performance in LHC Run 1*, submitted to Eur. Phys. J. (2016), arXiv: 1603.02934 [hep-ex].

[27] M. Cacciari and G. P. Salam, *Dispelling the N^3 myth for the k_t jet-finder*, Phys. Lett. **B641** (2006) 057, arXiv: hep-ph/0512210.

[28] M. Cacciari, G. P. Salam and G. Soyez, *FastJet User Manual*, Eur. Phys. J. **C 72** (2012) 1896, arXiv: 1111.6097 [hep-ph].

[29] D. Krohn, J. Thaler and L.-T. Wang, *Jet Trimming*, JHEP **02** (2010) 084, arXiv: 0912.1342 [hep-ph].

[30] S. Catani et al., *Longitudinally invariant K_t clustering algorithms for hadron hadron collisions*, Nucl. Phys. **B406** (1993) 187.

[31] ATLAS Collaboration, *Performance of jet substructure techniques for large-R jets in proton–proton collisions at $\sqrt{s} = 7$ TeV using the ATLAS detector*, JHEP **09** (2013) 076, arXiv: 1306.4945 [hep-ex].

[32] ATLAS Collaboration, *Identification of Boosted, Hadronically-Decaying W and Z Bosons in $\sqrt{s} = 13$ TeV Monte Carlo Simulations for ATLAS*, ATL-PHYS-PUB-2015-033, 2015, URL: http://cdsweb.cern.ch/record/2041461.

[33] ATLAS Collaboration, *Performance of b-Jet Identification in the ATLAS Experiment*, JINST **11** (2016) P04008, arXiv: 1512.01094 [hep-ex].

[34] M. Cacciari and G. P. Salam, *Pileup subtraction using jet areas*, Phys. Lett. **B659** (2008) 119, arXiv: 0707.1378 [hep-ph].

[35] ATLAS Collaboration, *Performance of jet substructure techniques for large-R jets in proton-proton collisions at* $\sqrt{s} = 7$ *TeV using the ATLAS detector*, J. High Energy Phys. **09** (2013) 076.

[36] M. Cacciari, G. P. Salam and G. Soyez, *The Catchment Area of Jets*, JHEP **0804** (2008) 005, arXiv: 0802.1188 [hep-ph].

[37] ATLAS Collaboration, *Optimisation of the ATLAS b-tagging performance for the 2016 LHC Run*, ATL-PHYS-PUB-2016-012, 2016, URL: https://cds.cern.ch/record/2160731.

[38] ATLAS Collaboration, *Jet mass reconstruction with the ATLAS Detector in early Run 2 data*, ATLAS-CONF-2016-035, 2016, URL: https://cds.cern.ch/record/2200211.

[39] A. J. Larkoski, G. P. Salam and J. Thaler, *Energy Correlation Functions for Jet Substructure*, JHEP **06** (2013) 108, arXiv: 1305.0007 [hep-ph].

[40] A. J. Larkoski, I. Mount and D. Neill, *Power Counting to Better Jet Observables*, JHEP **12** (2014) 009, arXiv: 1409.6298 [hep-ph].

[41] ATLAS Collaboration, *Identification of high transverse momentum top quarks in pp collisions at* $\sqrt{s} = 8$ *TeV with the ATLAS detector*, ATLAS-CONF-2015-036, 2015, URL: http://cdsweb.cern.ch/record/2043862.

[42] ATLAS Collaboration, *Studies of b-tagging performance and jet substructure in a high* p_{T} $g \to b\bar{b}$ *rich sample of large-R jets from pp collisions at* $\sqrt{s} = 8$ *TeV with the ATLAS detector*, ATLAS-CONF-2016-002, 2016, URL: http://cdsweb.cern.ch/record/2135187.

[43] ATLAS Collaboration, *Early Inner Detector Tracking Performance in the 2015 Data at* $\sqrt{s} = 13$ *TeV*, ATL-PHYS-PUB-2015-051, 2015, URL: http://cdsweb.cern.ch/record/2110140.

[44] ATLAS Collaboration, *Studies of the ATLAS Inner Detector material using* $\sqrt{s} = 13$ *TeV pp collision data*, ATL-PHYS-PUB-2015-050, 2015, URL: http://cdsweb.cern.ch/record/2109010.